Gauge-invariant treatment of gravitational radiation near the source: Analysis and numerical simulations

Andrew M. Abrahams
Center for Radiophysics and Space Research, Cornell University, Ithaca, New York 14853

Charles R. Evans
Department of Physics and Astronomy, University of North Carolina, Chapel Hill, North Carolina 27599
(Received 22 June 1990)

We discuss a procedure based on the use of multipole-moment expansions for matching numerical solutions for the gravitational-radiation field around a compact source to linear analytic solutions. Gauge-invariant perturbation theory is used to generate even- and odd-parity matching equations for each spherical harmonic order l,m. This technique determines asymptotic wave forms, valid in the local wave zone, from the numerically evolved fields in a weak-field annular region surrounding the isolated source. The separation of the wave form from near-zone and residual gauge effects is demonstrated using fully general-relativistic simulations of relativistic stars undergoing nonradial pulsation.

I. INTRODUCTION

This paper is concerned with the following question: How accurately can gravitational-radiation wave forms, emitted by an isolated strong-field source, be determined from spacelike $3+1$ numerical relativity simulations? We find that by using analytic-numerical matching techniques in conjunction with the simulations the answer is remarkably well.

By making some physically reasonable assumptions (which we discuss below), we devise several schemes [one of which was described in a previous paper[1] (hereafter paper I)] that extract an estimate of the asymptotic wave form from numerical values of the metric that are available in the outer regions of the computational domain. These assumptions are then validated (i) by empirically demonstrating that each method extracts mutually self-consistent wave forms from different radii outside the source, (ii) by empirically demonstrating that three independent methods mutually agree, and (iii) by showing that these internally consistent estimates of the wave form also agree with results obtained previously through perturbation calculations.[2]

A. Local wave zone surrounding an isolated source

The conceptual approach we adopt toward treating gravitational radiation has been developed by Thorne[3,5] in a series of articles. A key concept involves being able to characterize certain sources of gravity waves as *isolated*. To do this requires first splitting the spacetime around the source into a set of physically distinct spherical or annular regions. In order of increasing distance from the source, Thorne[3] identifies these as a strong-field interior ($r \lesssim 10M$), a weak-field near zone ($10M \lesssim r$ and $r \lesssim \lambda\!\!\!^{-}$), a local wave zone, and a distant wave zone.[4] The local wave zone is defined as the annular region ($r_I \lesssim r \lesssim r_O$) within which there are weak perturbations that behave as outgoing waves ($r \gg \lambda\!\!\!^{-}$) and throughout which the effects of background curvature are negligible.[3] The outer edge of the local wave zone (inner edge of the distant wave zone) at r_O is reached once the cumulative phase shift of the wave (produced by the M/r part of the source field) can no longer be ignored. A local wave zone may not surround all conceivable sources, but if it does exist, the source is considered to be isolated. Under the above assumptions one ignores within the local wave zone the differences between curved- and flat-space characteristics. Within this conceptual framework, Thorne splits the treatment of gravitational radiation into two parts: (i) calculation of the generation of the gravitational waves and their propagation into the local wave zone and (ii) propagation of the gravitational radiation from the local wave zone out through the distant wave zone to the observer.

The axisymmetric, two-dimensional (2D) numerical relativity simulations, which are used for exploring the radiation extraction schemes described in this paper, perform the tasks of calculating the generation of the gravitational waves in the strong-field interior and propagating the waves out to the inner edge of the local wave zone. The gauge that is used for these simulations is asymptotically Minkowskian, but because the outer edge of the computational domain rarely extends beyond $r \sim 250M$, we never deal with the delicate issue of choosing coordinates that avoid logarithmic divergences associated with distant wave propagation on a curved background. The matching schemes described in this paper and in paper I apply in the local wave zone and in the weak-field near zone (a portion of this region overlaps the computational domain of the simulation).

It is important to emphasize that the purpose of the matching schemes we have developed is *not* to treat the propagation of the waves from the local wave zone through the distant wave zone. Instead, their primary purpose is to determine from the time-varying fields at

the inner edge of local wave zone or from the near-zone fields (where $r \lesssim \lambda$) the wave form to be expected in the more distant portions of the *local* wave zone ($r \gg \lambda$ and $r \gg M$). Typical numerical relativity simulations do not have computational domains that extend to $r \gg \lambda$ so the metric variables include near-zone and linear gauge effects even at the outer edge of the grid. Hence it is necessary to extract from these complicated fields the "asymptotic" wave forms that would emerge further out in the local wave zone once these nonradiative effects become negligible.

The precise behavior of the waves as they propagate from the local wave zone to the observer depends on intervening sources that perturb the propagation. (In general, these effects can be treated using geometrical optics.[4]) Despite the fact that we are not treating this more distant propagation problem, we nonetheless expect that for many sources the wave forms we extract will provide an accurate indication of the wave forms that a distant detector would see, up to large, unobservable phase shifts. As mentioned above, some proof of this conjecture is provided by the simulations we make of small- but finite-amplitude pulsations of relativistic stars. In Sec. III we compare the wave forms we extract and the implied damping times of the oscillations with the results from previous perturbation calculations of pulsating relativistic stars.

B. Gauge-invariant approaches to matching

Any matching procedure that attempts to determine what wave form will emerge from the fields in the near zone or the inner edge of the local wave zone must do two things. First, the complicated time-dependent effects of the gauge that is used in the numerical relativity algorithm must be separated off. For reasonable gauge choices the effects progressively die off with increasing radius as the coordinates become Minkowskian, but are usually non-negligible within the computational domain. After this step what remains in the weak-field region, for those multipoles with $l \geq 2$, is a linear combination of the wave form and the nonradiative near-zone field. Thus the second task of the matching technique is to separate off the wave form from the nonradiative part of the field.

In paper I we derived an analytic formalism for making these two separations. The essential assumption was that within the local wave zone and the weak-field near zone the use of flat-space characteristics is an adequate approximation. With Minkowskii space as the assumed background in this annular region, one may write out[1,3] a general multipole-moment solution to the equations of linearized gravity, which includes static and time-dependent moments (waves). This solution is worked out in a particular gauge, but can be transformed to any other asymptotically Minkowskii gauge. By transforming the solution to the gauge used in the numerical relativity simulation, we were able to identify how gauge effects entered into the multipole amplitudes. It was then possible to construct suitable linear combinations of the amplitudes derived from a decomposition of the spatial metric h_{ij} that were free of these gauge influences and contained only a dependence on the wave and its near-zone field (for $l \geq 2$). Finally, the asymptotically radiative part of the field (the wave form) is separated from the near-zone field by integrating an ordinary differential equation (ODE) in time at a fixed radius.

The most significant drawback of this "template" matching method is that it requires the user to have a detailed knowledge of the asymptotic behavior of the gauge that is used for the simulation and of the form of the multipole-moment solution in that gauge. The matching was worked out[1] for two commonly used numerical relativity gauges: quasi-isotropic gauge and radial gauge.

Since not all numerical relativists may choose to use one of these two gauges, it is important to consider how a gauge-nonspecific extraction method might be defined. In Sec. II we present in detail one such gauge-invariant approach for matching numerical data to the analytic solution. The scheme is based in part upon an idea of Moncrief[6] who demonstrated how gauge-invariant variables can be constructed at each order in a multipole expansion. The particular gauge-invariant technique we construct is straightforward to implement and should work for any asymptotically Minkowskii gauge, provided that a suitable weak-field region is available surrounding the strong-field source. A second gauge-invariant procedure (a variant of one presented in paper I) based upon calculating moments of Riemann tensor components is described in Appendix B.

We show in Sec. IV how the numerical matching extracts a consistent estimate of the wave form by employing the gauge-invariant technique as part of a set of numerical simulations. These simulations involve calculating spacetimes that consist of a relativistic star oscillating with finite amplitude in one or more nonradial modes and emitting gravitational waves. Internal consistency is demonstrated by comparing the wave forms extracted from different radii in the weak-field region of the computational domain. We also demonstrate the inadequacy of standard metric variables for reading off the wave form. First, however, in Sec. III, we describe how the simulations are initialized to calculate these radiative spacetimes and how the wave forms we obtain agree with previous independent perturbation calculations of infinitesimal pulsations. Appendix A describes how multipole decomposition of the initial data can be used to provide initial values of the moments required to perform the ODE integrations that are part of the extraction process.

II. GAUGE-INVARIANT MATCHING

Moncrief[6] has constructed a set of gauge-invariant variables useful in studying small radiative perturbations of the Schwarzschild metric. These gauge-invariant variables are constructed from the amplitudes obtained in a multipole-moment decomposition of the metric using Regge-Wheeler harmonics. At a given order l,m the Regge-Wheeler perturbation variables are each subject to changes under the action of an arbitrary infinitesimal gauge transformation on the Schwarzschild background. Moncrief has shown, however, that certain linear com-

binations of the multipole-moment amplitudes and their first radial derivatives are invariant with respect to infinitesimal gauge transformations. At each order l,m there are two unconstrained gauge-invariant variables: one with even parity and one with odd parity. Moncrief has shown that these functions satisfy the Zerilli and Regge-Wheeler equations, respectively, and thereby encode information on the wave form.

An even simpler procedure for constructing gauge-invariant variables can be developed by using a multipole-moment decomposition of perturbations in linearized gravity. The reason for using linearized gravity, and Minkowskii spacetime as the background, is that it is then possible[1] to write down a general analytic solution to the perturbation equations. In any case, this approximation is consistent with the assumptions underlying the identification of a local wave zone. Using this solution, the analytic forms of the two gauge-invariant variables can be computed. We then fashion a gauge-invariant means of matching a numerically calculated metric to the analytic solution and thereby extract an estimate of the asymptotic gravitational-radiation wave form.

As in paper I, we assume that outside of a strong-field source, in the weak-field region, the metric can be given in terms of a perturbation $h_{\alpha\beta}$ about Minkowskii space:

$$g_{\alpha\beta}=\eta_{\alpha\beta}+h_{\alpha\beta} . \tag{1}$$

The equations of linearized gravity in the Lorentz gauge are

$$-\partial_t^2\bar{h}_{\alpha\beta}+\nabla_k\nabla_k\bar{h}_{\alpha\beta}=0 , \tag{2a}$$

$$\partial_t\bar{h}_{\alpha t}=\nabla_k\bar{h}_{\alpha k} , \tag{2b}$$

where the trace-reversed perturbation (gravitational field[7]) is $\bar{h}_{\alpha\beta}=h_{\alpha\beta}-\frac{1}{2}\eta_{\alpha\beta}\eta^{\gamma\delta}h_{\gamma\delta}$. To express these equations we use spherical orthonormal components. Greek indices run from 0 to 3 and Latin indices from 1 to 3. We use geometrized units ($G=c=1$) unless otherwise noted, and our metric signature is $+2$. The three-dimensional flat-space covariant derivative is ∇_k.

In paper I we gave the general multipole-moment solution to (2a) and (2b) expressed in a particular subgauge of the Lorentz gauge we call the Lorentz-Thorne gauge. In terms of pure-orbit tensor spherical harmonics,[1,3] the spatial part of the metric for a given l and m ($l\geq 2$) is

$$\begin{aligned} h_{ij}^{(lm)}=&-\left[\frac{3l(l-1)}{2(l+1)(l+2)}\right]^{1/2}\{\mathcal{I}_{lm}^{(l)}\}_l T_{ij}^{0\,l,lm} \\ &+\left[\frac{2(2l-1)(2l+1)}{(l+1)(l+2)}\right]^{1/2}\{\mathcal{I}_{lm}^{(l)}\}_{l-2}T_{ij}^{2\,l-2,lm} \\ &+i\left[\frac{2l+1}{l+2}\right]^{1/2}\{\mathcal{S}_{lm}^{(l)}\}_{l-1}T_{ij}^{2\,l-1,lm} . \end{aligned} \tag{3}$$

At each order l and m there is a mass moment $\mathcal{I}_{lm}(t-\epsilon r)$ and a current moment $\mathcal{S}_{lm}(t-\epsilon r)$ that are functions only of retarded ($\epsilon=+1$) or advanced ($\epsilon=-1$) time. The curly brackets (Burke functionals[1,8]) denote combinations of derivatives of these moments and powers of r, which are solutions to the radial wave equation (see paper I, Appendix); superscripts denote derivatives with respect to $t-\epsilon r$.

The moments are specified in (3) so that asymptotically the metric becomes (for a given l and m)

$$h_{ij}^{TT}\simeq\frac{\mathcal{I}_{lm}^{(l)}(t-\epsilon r)}{r}T_{ij}^{E2,lm}+\frac{\mathcal{S}_{lm}^{(l)}(t-\epsilon r)}{r}T_{ij}^{B2,lm} , \tag{4}$$

where $T_{ij}^{E2,lm}$ and $T_{ij}^{B2,lm}$ are transverse-traceless pure-spin harmonics.

In an arbitrary gauge, the metric perturbation of order $l\geq 2$ and m, including both even- and odd-parity parts, can be written as

$$\begin{aligned} h_{ij}^{(lm)}=&A_{0\,l,lm}\tilde{T}_{ij}^{0\,l,lm}+A_{2\,l-2,lm}\tilde{T}_{ij}^{2\,l-2,lm} \\ &+A_{2\,l-1,lm}\tilde{T}_{ij}^{2\,l-1,lm}+A_{2\,l,lm}\tilde{T}_{ij}^{2\,l,lm} \\ &+A_{2\,l+1,lm}\tilde{T}_{ij}^{2\,l+1,lm}+A_{2\,l+2,lm}\tilde{T}_{ij}^{2\,l+2,lm} , \end{aligned} \tag{5}$$

where the $\tilde{T}_{ij}^{\lambda\,l',lm}$ are scaled pure-orbit tensor spherical harmonics.[1,3] Now consider an infinitesimal gauge transformation of the metric:

$$h'_{ij}=h_{ij}+\nabla_i\zeta_j+\nabla_j\zeta_i . \tag{6}$$

Since this gauge transformation is linear, it can be decomposed into multipole moments; for a particular order l,m the generator ζ_i has the general form

$$\begin{aligned} \zeta_i^{(lm)}=&\Phi_{l-1,lm}\tilde{Y}_i^{l-1,lm}+\Phi_{l,lm}\tilde{Y}_i^{l,lm} \\ &+\Phi_{l+1,lm}\tilde{Y}_i^{l+1,lm} . \end{aligned} \tag{7}$$

The transformation (6) then induces the following changes in the amplitudes found in Eq. (5) [see paper I, Eq. (A25)]:

$$\delta A_{0\,l,lm}=\tfrac{2}{3}D_{l-1}^{+}\Phi_{l-1,lm}-\tfrac{2}{3}D_{l+1}^{-}\Phi_{l+1,lm} , \tag{8a}$$

$$\delta A_{2\,l-2,lm}=\frac{2(l-1)}{2l-1}D_{l-1}^{-}\Phi_{l-1,lm} , \tag{8b}$$

$$\delta A_{2\,l-1,lm}=-\frac{2(l-1)}{2l+1}D_{l}^{-}\Phi_{l,lm} , \tag{8c}$$

$$\begin{aligned} \delta A_{2\,l,lm}=&\frac{2(l+1)}{3(2l-1)}D_{l-1}^{+}\Phi_{l-1,lm} \\ &-\frac{2l}{3(2l+3)}D_{l+1}^{-}\Phi_{l+1,lm} , \end{aligned} \tag{8d}$$

$$\delta A_{2\,l+1,lm}=-\frac{2(l+2)}{2l+1}D_{l}^{+}\Phi_{l,lm} , \tag{8e}$$

$$\delta A_{2\,l+2,lm}=-\frac{2(l+2)}{2l+3}D_{l+1}^{+}\Phi_{l+1,lm} , \tag{8f}$$

where $D_l^{+}=\partial_r-l/r$ and $D_l^{-}=\partial_r+(l+1)/r$ act as angular momentum raising and lowering operators on solutions of the radial wave equation.

Using these transformations, we follow Moncrief and construct two unconstrained gauge invariants. It is easy to combine the odd-parity amplitudes $A_{2\,l-1,lm}$ and $A_{2\,l+1,lm}$ and their radial derivatives to form a variable

$$Q_o^{(lm)} = -A_{2l-1,lm} - A_{2l+1,lm} + \frac{1}{l-1} r\partial_r A_{2l-1,lm} - \frac{1}{l+2} r\partial_r A_{2l+1,lm} , \quad (9)$$

which is invariant ($\delta Q_o^{(lm)}=0$) with respect to the changes induced by Eq. (6). Furthermore, this odd-parity gauge-invariant variable is not subject to any of the field constraints (e.g., the Hamiltonian constraint).

For even-parity perturbations it is possible to find two gauge-invariant combinations of the remaining four amplitudes. There is a particular combination of these two gauge-invariant variables,

$$\begin{aligned} Q_e^{(lm)} = {} & l(l+1)A_{0l,lm} - (l-2)A_{2l-2,lm} \\ & - (2l^2+2l-3)A_{2l,lm} + (l+3)A_{2l+2,lm} \\ & - 2r\partial_r A_{0l,lm} + r\partial_r A_{2l-2,lm} \\ & + r\partial_r A_{2l,lm} + r\partial_r A_{2l+2,lm} , \end{aligned} \quad (10)$$

which is not constrained by the Hamiltonian constraint.

In order to use these invariants as the basis of a radiation extraction method, we first calculate them in the gauge in which our analytic matching solution is written. Using the solution (3), we arrive at the matching equations

$$Q_o^{(lm)}(t;r) = \frac{2}{l(l+2)} \epsilon r \{S_{lm}^{(l+1)}\}_l \quad (11)$$

and

$$Q_e^{(lm)}(t;r) = l(l+2)\{I_{lm}^{(l)}\}_l , \quad (12)$$

where

$$\begin{aligned} I_{lm} &= \left[\frac{(l+1)(l-1)(2l+1)}{8\pi l(l+2)} \right]^{1/2} \mathcal{I}_{lm} , \\ S_{lm} &= \left[\frac{(l+2)(2l+1)l}{8\pi(l-1)(l+1)} \right]^{1/2} \mathcal{S}_{lm} \end{aligned} \quad (13)$$

are convenient rescalings of the mass and current moments.[1] It should be remembered that since these variables are gauge invariant, the weak-field solution obtained in *any* gauge [e.g., transverse-traceless (TT) gauge] would produce the same dependence in $Q_o^{(lm)}$ and $Q_e^{(lm)}$.

In order to use the matching equations [Eqs. (11) and (12)], the gauge-invariant variables $Q_e^{(lm)}$ and $Q_o^{(lm)}$ have to be calculated from data available in a simulation. To find these, we must first obtain the amplitudes $A_{\lambda l',lm}$ and $r\partial_r A_{\lambda l',lm}$ by calculating the surface integrals[1]

$$A_{\lambda l',lm} = \frac{1}{d_{\lambda l',l}} \int d\Omega\, h_{ij}(r_0)(T_{ij}^{\lambda l',lm})^* , \quad (14a)$$

$$(r\partial_r A_{\lambda l',lm})_{r=r_0} = \frac{r_0}{d_{\lambda l',l}} \int d\Omega\, \partial_r h_{ij}(r_0)(T_{ij}^{\lambda l',lm})^* , \quad (14b)$$

at an arbitrary radius $r=r_0$ in the weak-field region. The $Q_e^{(lm)}$ and $Q_o^{(lm)}$ determined from a given spacetime will not depend upon the gauge used in the simulation to first order.

The gauge-invariant amplitudes calculated numerically using (9) and (10) serve as source terms in (11) and (12). Knowing $Q_e^{(lm)}$ and $Q_o^{(lm)}$ as time series at a given radius, Eqs. (11) and (12) become ordinary differential equations for the mass and current moments. As we discuss in paper I, integration of these ODE's along a timelike cylinder separates the wave forms from the near-zone field.

To further illustrate this matching technique, let us consider two concrete examples. Assuming axisymmetry ($m=0$), Eqs. (11) and (12) for the mass quadrupole moment ($l=2$) and the current octupole moment ($l=3$) (equatorial plane symmetry allows only even-l mass moments and odd-l current moments) are

$$I^{(2)}(t-r_0) + 3\frac{I^{(1)}(t-r_0)}{r_0} + 3\frac{I(t-r_0)}{r_0^2} = \frac{r_0}{8} Q_e^{(l=2)}(t;r_0) , \quad (15a)$$

and

$$S^{(4)}(t-r_0) + 6\frac{S^{(3)}(t-r_0)}{r_0} + 15\frac{S^{(2)}(t-r_0)}{r_0^2} + 15\frac{S^{(1)}(t-r_0)}{r_0^3} = \frac{15}{2} Q_o^{(l=3)}(t;r_0) . \quad (15b)$$

The gauge-invariant amplitudes to be numerically evaluated are [Eqs. (9) and (10)]

$$\begin{aligned} Q_e^{(l=2)} = {} & 6A_{02,2} - 9A_{22,2} + 5A_{24,2} \\ & - 2r\partial_r A_{02,2} + r\partial_r A_{20,2} + r\partial_r A_{22,2} \\ & + r\partial_r A_{24,2}|_{r=r_0} , \end{aligned} \quad (16a)$$

$$\begin{aligned} Q_o^{(l=3)} = {} & -A_{22,3} - A_{24,3} + \tfrac{1}{2} r\partial_r A_{22,3} \\ & - \tfrac{1}{5} r\partial_r A_{24,3}|_{r=r_0} . \end{aligned} \quad (16b)$$

We have assumed in these expressions that only outgoing radiation $\epsilon=+1$ is present. The utility of Eqs. (15a) and (16a) for extracting the asymptotic even-parity quadrupole wave form is examined in Sec. IV.

III. PHYSICAL MODEL AND CODE

Nonradial pulsating neutron-star spacetimes provide an excellent environment in which to examine our radiation extraction techniques. The neutron star provides both a source of gravitational radiation and an approximately static mass-monopole moment creating a vacuum Schwarzschild background upon which the waves propagate. For this physical configuration the strong-field interior, near zone, local wave zone, and distant wave zone are easily delineated. In addition, in the limit of small-amplitude oscillations, the numerical simulations can be compared to the extensive perturbation-theory studies[2,9] to provide an external check on the reliability of the simulations and extraction techniques.

The simulations of the pulsating neutron-star spacetime are calculated using a code that solves the axisymmetric (2D) equations for the general-relativistic gravitational field and hydrodynamics.[10] The Einstein equations are solved by using the spacelike 3+1 approach and by employing as coordinates the quasi-isotropic (QI) spatial gauge and the maximal time-slicing condition. In the QI gauge the spatial line element may be written as

$$ds^2=\phi^4[e^{2\eta/3}(dr^2+r^2d\theta^2)+e^{-4\eta/3}r^2(\sin\theta d\phi+\xi d\theta)^2] , \tag{17}$$

in terms of the conformal factor ϕ and the even- and odd-parity "radiative" variables η and ξ. These variables are singled out because the mass monopole does not appear in their asymptotic expansions. The conformal factor ϕ is found by solving the Hamiltonian constraint equation, and this is one of the steps required to start the simulation off with proper initial data. Further details on the gravitational field equations and the relativistic hydrodynamic equations that are solved by the finite-difference code can be found elsewhere.[10]

A. Initial data for pulsating relativistic stars

The initial data for the oscillating neutron-star evolution are established as follows. First, an equilibrium relativistic stellar model with the desired central energy density w_c is calculated by solving the Tolman-Oppenheimer-Volkov (TOV) equation using a tabulated nuclear equation of state.[2] Then the star is taken out of hydrostatic equilibrium by distorting it with an even-parity displacement vector defined by

$$\xi^r=A_l r^{-2}P_l(\cos\theta)W_l(r) , \tag{18a}$$

$$\xi^\theta=\frac{A_l}{l}r^{-2}\partial_\theta P_l(\cos\theta)V_l(r) . \tag{18b}$$

Up to satisfying the regularity condition at $r=0$ ($W_l\sim r^{l+1}$ and $V_l\sim r^l$), the radial functions W_l and V_l are arbitrary. We parametrize these functions in a way that is reminiscent of the trial functions used by Detweiler and Ipser[11] in their variational calculations:

$$W_l(r)=r^{l+1}\left[1+a_l\left[\frac{r}{R}\right]^2\right], \quad V_l(r)=r^l\left[1+b_l\left[\frac{r}{R}\right]^2\right] , \tag{19}$$

where R is the stellar radius, and a_l and b_l are constants. The values chosen for the constants a_l and b_l determine the relative excitation of the quasinormal (p) modes of the star. We restrict attention in this paper to quadrupole ($l=2$) displacements only. For a suitable choice of values for a_2 and b_2, it is possible to excite almost exclusively the quadrupole f mode of the star. We use this choice in our comparison (Sec. III B) with perturbation theory. Alternatively, it is possible to excite strongly several quadrupole overtones, and we also use such a model in Sec. IV in examining the extraction scheme.

Once the stellar density and energy density have been displaced using (18), the velocity is initialized to vanish (moment of time symmetry) and hence the extrinsic curvature initially vanishes $K_{ij}=0$. We then take the three-geometry of the initial slice to be conformally flat and finally solve the Hamiltonian constraint for ϕ to complete the specification of proper initial data. One of the apparent results of choosing a conformally flat initial slice is that there is very little radiation initially present in the vacuum regions outside the star. As the evolution begins, the hydrodynamic oscillation of the star drives a wave train outward with a relatively sharp front. As the wave reaches the edge of the computational mesh, an outgoing boundary condition is applied which minimizes the reflected return.

B. Comparison with perturbation theory

Perturbation calculations of nonradial oscillations of relativistic stars yield two fundamental numbers: the frequency of an eigenmode and its damping rate (imaginary part of frequency) due to emission of gravitational radiation. Within a few oscillation periods, our finite-amplitude calculations allow the frequency to be determined. However, direct determination of the damping rate of the mode is not feasible since numerical dissipation dominates radiation damping of the oscillation by at least 2 orders of magnitude. Instead, we calculate the damping time indirectly by employing one of the techniques outlined by Thorne.[12] This technique relies upon calculating the energy of the pulsation, E_M, as measured by a distant observer. As the star oscillates, E_M passes back and forth between kinetic and potential energies. When $\xi=0$, E_M is equal to the kinetic energy:

$$E_M=\tfrac{1}{2}\int d^3x\,\gamma^{1/2}\alpha\rho h\gamma^{ij}U_iU_j , \tag{20}$$

where the integral includes contributions from the total inertial energy density $\rho h=\rho+\rho\epsilon+p$, the gravitational redshift (lapse function α), and the proper velocity.

The energy in the pulsation, E_M, is then compared to E_W, the energy radiated per wavelength. For quadrupole waves E_W is given by

$$E_W=\frac{2\pi}{15}\lambda\!\!\!^{-1}A^2 , \tag{21}$$

where A is the amplitude of the extracted quadrupole wave form. With the total pulsation energy and rate of energy loss through radiation, we arrive at the damping time

$$\tau_{\rm damp}=4\pi\lambda\!\!\!^{-}\frac{E_M}{E_W}=30\lambda\!\!\!^{-2}\frac{E_M}{A^2} . \tag{22}$$

In Table I, we show results from our small but finite-amplitude stellar pulsation simulations. These stellar models were constructed by using the Harrison-Wakano-Wheeler (HWW) equation of state and adopting three different central densities.[13] We identify radial ($l=0$), f-mode frequencies from the lapse function, measure quadrupole ($l=2$) f-mode frequencies from the emitted waveforms, and infer quadrupole damping times τ. Where possible these are compared to values obtained from perturbation calculations.[2,9]

TABLE I. Relativistic neutron-star pulsation tests. Data extracted from fully general-relativistic simulations are compared against perturbation-theory results for $l=0$ and 2 fundamental mode frequencies and damping times. We show results for the HWW (Ref. 13) equation of state and three different values of the central energy density w_c.

w_c	Source	f ($l=0$) (kHz)	f ($l=2$) (kHz)	τ_{damp} (s)
3.0×10^{15}	Code	1.5	2.38	0.32
	(Ref. 2)		2.43	0.300
	(Ref. 9)	1.23		
1.0×10^{15}	Code	1.1	1.4	1.4
	(Ref. 2)		1.47	1.28
3.0×10^{14}	Code	0.77	0.83	8.0
	(Ref. 2)		0.835	7.43
	(Ref. 9)	0.794		

IV. APPLICATIONS OF RADIATION EXTRACTION

Using the extraction methods is quite straightforward. For most of the discussion in this section, we limit attention to the gauge-invariant scheme given in Sec. II. It should be possible to employ this scheme in numerical relativity calculations that use most any gauge. We have also found it to be the most internally consistent of the three methods. (Implementation of the template method is described in paper I and the Riemann method is discussed in Appendix B.)

To extract the even-parity wave form requires computation [Eq. (10)] of eight multipole amplitudes over the metric at a fixed coordinate radius: $A_{\lambda l',lm}$ and their first radial derivatives $\partial_r A_{\lambda l',lm}$. These multipole amplitudes are combined to form the gauge-invariant amplitude $Q_e^{(lm)}$. By equating this numerically derived time series to the analytic form of $Q_e^{(lm)}$ [Eq. (12)], an ordinary differential equation is obtained whose solution completes the extraction at a fixed radius. For the quadrupole case, the ODE [Eq. (15a) with Eq. (16a) as the source] is second order. This process can be repeated at any number of radii.

The extraction ODE for the quadrupole moment is solved by splitting it into first-order form and integrating it using the time-step size set by the simulation and employing a second-order accurate finite-difference calculation. While the time integration of this extraction equation requires initial values for the quadrupole moment I and its first time derivative $I^{(1)}$, we have made no attempt to employ initial values calculated from the Cauchy data for these simulations. In Appendix A, we demonstrate that it is possible in principle to calculate these initial values. However, as we showed previously,[14] the initial values appear as transient contributions that die off exponentially with e-folding times on the order of the light-crossing time of the extraction radius. Consequently, for practical applications where small extraction radii are used, errors in these initial values will have little effect on the extracted asymptotic wave form.

A. Extraction of the wave forms

We consider two pulsating neutron-star models. The first model is an attempt to excite just the quadrupole f-mode oscillation. To do this we choose the displacement (18) by setting $a_2=4.0$ and $b_2=3.0$ in (19). The second model has a displacement vector that is chosen to excite several of the lowest quadrupole p modes as well as the f mode. For this multimode model we took $a_2=-10.0$ and $b_2=-3.0$. The overall amplitude of the oscillations was set by taking $A_2=0.005$ in both cases. We employ the HWW equation of state with a central mass-energy density of 1.0×10^{15} g cm^{-3}.

To evaluate the emitted gravitational waves, we placed five "numerical detectors" at radii of $r_0\simeq\lambda\!\!\!^{-}/2$, $\lambda\!\!\!^{-}$, $2\lambda\!\!\!^{-}$, $4\lambda\!\!\!^{-}$, and $6\lambda\!\!\!^{-}$, where $\lambda\!\!\!^{-}\simeq25M$ is the reduced wavelength of the $l=2$ fundamental mode for this stellar model. The numerical grid extended out to a radius of $180M$ and the finite-difference mesh contained 180 radial zones and 16 angular zones over a single polar quadrant. In these simulations our units are such that $1M$ corresponds to one solar mass.

In Fig. 1 we show for both runs the time-dependent behavior of the radiative variable η (along the equator $\sin\theta=1$). In each case results are shown for the five different extraction radii with the values plotted against flat-space retarded time $t-r_0$. There is considerable disagreement between the "wave forms" obtained at different radii, and there is no clear convergence of the wave forms as one would expect to occur further out in the local wave zone. We conclude that trying to read off the wave from the metric alone is not a good idea at these too-small distances from the source.

The reasons why η fails to provide a suitable deter-

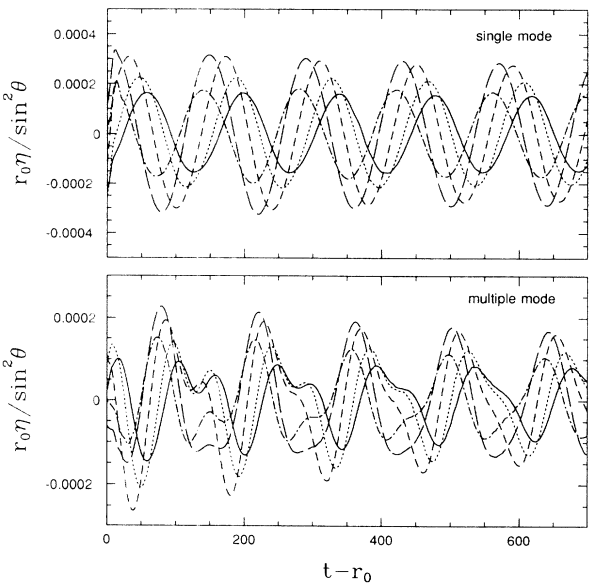

FIG. 1. Results are shown for a single-mode run (upper panel) and a multiple-mode run (lower panel). The radiative metric variable $r_0\eta/\sin^2\theta$ is plotted as a function of flat-space retarded time $t-r_0$ (in M) at five radii: $r_0\simeq12.5M$ (solid), $r_0\simeq25M$ (dotted), $r_0\simeq50M$ (short-dashed), $r_0\simeq100M$ (long-dashed), and $r_0\simeq150M$ (dashed and dotted).

mination of the asymptotic wave form can be understood by examining its weak-field expansion in the QI gauge (including only multipoles with $l \leq 2$):

$$\eta = \sin^2\theta \left[\frac{I^{(2)}(t-r)}{r} + 2\frac{I^{(1)}(t-r)}{r^2} + \frac{b_2(t)}{r^2} \right] \quad (23)$$

(note that we assume above only an outgoing dependence $\epsilon = +1$). While η does display the leading-order radiative part $I^{(2)}(t-r)$, it also has a near-zone field term $I^{(1)}(t-r)$ and a gauge dependency $b_2(t)$ that arise because the QI gauge is fixed by elliptic conditions. Both the near-zone and gauge terms die off asymptotically relative to the radiative term, but they are not negligible at the radii used in these simulations.

The gauge dependence can be eliminated by calculating the gauge-invariant amplitude $r_0 Q_e^{(l=2)}(t;r_0)$ using Eq. (16a). We plot this amplitude for both runs and all five extraction radii in Fig. 2. These amplitudes are even less indicative of an asymptotic wave form mainly because the near-zone field is more pronounced [compare Eqs. (15a) and (23)]. They do, however, exhibit a clear convergence toward larger radii. In Fig. 3 we compare the extracted wave forms found at the five different radii by integrating Eq. (15a) and separating off the near-zone field. The extracted wave forms agree in both amplitude and phase (when plotted against flat-space retarded time) to better than 5%. We expect that these wave forms represent (to the stated level of accuracy) those that would arrive in the local wave zone.

There is another way to see how the extraction procedure works and to what extent nonradiative effects are still present near the outer part of the computational domain. In Fig. 4, we present two plots of data obtained from just the multiple-mode run. The upper plot displays information obtained from the radius $r_0 \simeq 12.5M$, while the lower plot shows the same quantities obtained from a radius of $r_0 \simeq 100M$. The three curves plotted in each of these panels are the radiative metric variable

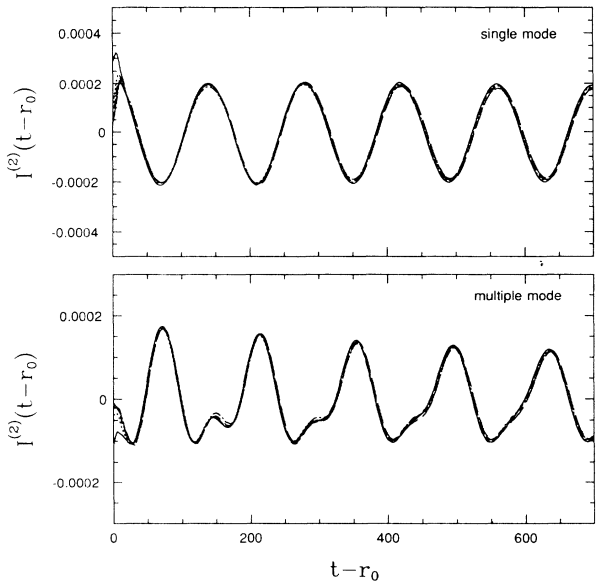

FIG. 3. Extracted second time derivative of the quadrupole moment (the asymptotic wave form) $I^{(2)}(t-r_0)$ is shown at five radii: $r_0 \simeq 12.5M$ (solid), $r_0 \simeq 25M$ (dotted), $r_0 \simeq 50M$ (short-dashed), $r_0 \simeq 100M$ (long-dashed), and $r_0 \simeq 150M$ (dashed and dotted). Again, results are shown for a single-mode run (upper panel) and a multiple-mode run (lower panel) and are plotted against $t-r_0$ (in M).

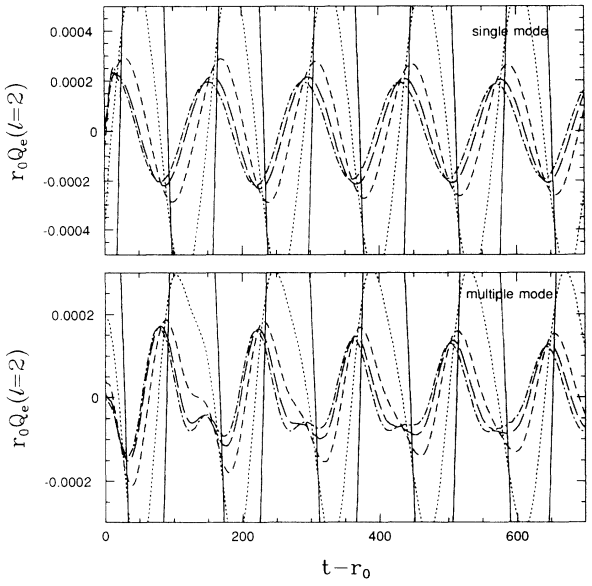

FIG. 2. Gauge-invariant amplitude $r_0 Q_e^{(l=2)}(t;r_0)$ is plotted as a function of flat-space retarded time (in M) at five radii: $r_0 \simeq 12.5M$ (solid), $r_0 \simeq 25M$ (dotted), $r_0 \simeq 50M$ (short-dashed), $r_0 \simeq 100M$ (long-dashed), and $r_0 \simeq 150M$ (dashed and dotted). Again, results are shown for a single-mode run (upper panel) and a multiple-mode run (lower panel).

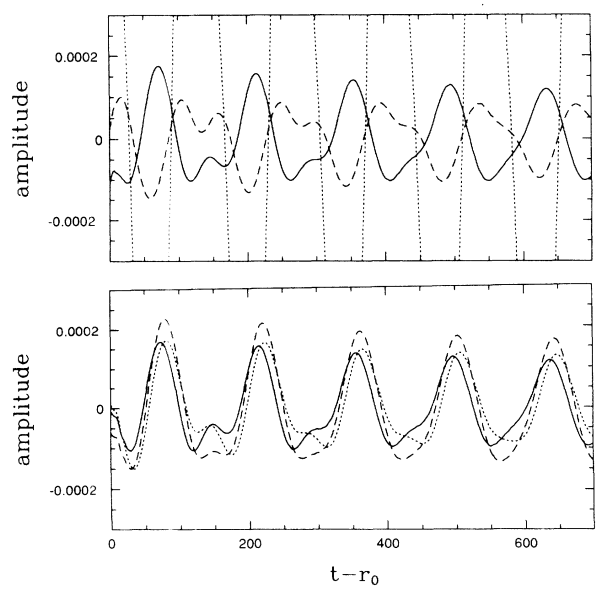

FIG. 4. Comparison between the radiative metric variable $r_0\eta/\sin^2\theta$ (dashed), the gauge-invariant amplitude $r_0 Q_e^{(l=2)}$ (dotted), and the extracted wave form $I^{(2)}(t-r_0)$ (solid), as functions of flat-space retarded time $t-r_0$ (in M) using the multiple-mode run. These comparisons are made at $r_0 \simeq 12.5M$ (upper panel) and at $r_0 \simeq 100M$ (lower panel).

$r_0\eta(t;r_0)/\sin^2\theta$, the gauge-invariant amplitude $r_0 Q_e^{(l=2)}(t;r_0)$, and the extracted second time derivative of the quadrupole moment $I^{(2)}(t-r_0)$. Since the lowest-frequency mode in these wave trains has a wavelength $\lambda \simeq 150M$, the inner radius lies within the near zone, while the outer radius ($r_0 \simeq 4\lambda$) lies within the inner edge of the local wave zone. The two sets of curves are plotted versus the same values of retarded time $t-r_0$.

At $r_0 \simeq 12.5M$ the effect of the near zone on $Q_e^{(l=2)}$ is quite pronounced. Interestingly, however, the overall amplitude of the radiative variable η is fairly close to that of the extracted wave form. This is an artifact of the elliptic nature of the QI gauge; the function b_2 arises as a homogeneous solution to the gauge-fixing equation the appearance of which guarantees regularity of the coordinates. In general, the value of b_2 is dependent on some measure of the rate of change of the quadrupole moment in the interior. For the special case of an everywhere weak-field configuration, b_2 is directly determined by the first time derivative of the quadrupole moment *evaluated at* $r=0$:

$$b(t) = -2I^{(1)}(t) . \tag{24}$$

Comparison with Eq. (23) shows that the gauge and near-zone terms in η nearly cancel in the interior or at small radii. The residual difference between $r\eta/\sin^2\theta$ and $I^{(2)}$ at $r_0 = 12.5$ is largely the result of the ~ 0.08 in phase offset of $r_0 = 12.5M$ from the origin. At $r_0 \simeq 100M$ the near-zone field has largely disappeared, and so there is considerable agreement between the overall amplitudes of the gauge-invariant function and final extracted wave form. The radiative variable η is also indicating convergence to the asymptotic wave form. Nonetheless, even at this distance from the source, the residual coordinate effects introduce considerable distortions between these quantities.

The effect of the near-zone field can be examined in another way. Consider the gauge-invariant amplitude $Q_e^{(l=2)}(t;r)$. This should tend asymptotically to the radiative term $I^{(2)}(t-r)/r$. For a sinusoidal wave form it is possible to calculate analytically the effect of the near-zone field terms on $Q_e^{(l=2)}(t;r)$. If the asymptotic wave form is assumed to have the form $I^{(2)}/r = A\sin[\lambda^{-1}(t-r)]/r$, then $Q_e^{(l=2)}(t;r)$ is expected to have the dependence

$$rQ_e^{(l=2)}(t;r) = A\left[1+3\left[\frac{\lambda}{r}\right]^2+9\left[\frac{\lambda}{r}\right]^4\right]^{1/2} \times \sin\left[\frac{t-r}{\lambda}+\psi\right], \tag{25}$$

where the phase shift is given by $\psi = \arctan[3r\lambda(3\lambda - r^2)^{-1}]$. One compares the analytic prediction for $rQ_e^{(l=2)}(t;r)/I^{(2)}(t-r)$ as a function of r against the same ratio obtained from the simulation. The results of this comparison[15] indicate that our analytic matching solution quite accurately describes the near-zone field in the region $\lambda/2 \le r_0 \le 6\lambda$.

B. Confidence checks

There are several other checks that give us confidence in these numerical calculations. As we showed in paper I, the multipole amplitude $A_{24,20}$ is identically zero in the QI gauge. This is satisfied numerically quite well: $|A_{24,20}/Q_e^{(l=2)}| < 10^{-5}$ in simulations with 16 angular zones (the angular zoning determines the degree of orthogonality in numerical representations of Legendre polynomials).

Figure 5 compares the wave forms extracted using the template and Riemann methods against the gauge-invariant method. For this comparison we use the multiple-mode run (with 290×16 grid resolution) and extract the wave forms at $r_0 \simeq 100M$. The fractional errors between these two schemes and the gauge-invariant scheme are less than 4% in the case of the template method and less than 1% for the Riemann method.

The convergence of the numerical simulations themselves is tested in Fig. 6, by varying the grid resolution and looking at the resulting changes in the wave forms. We examine the wave forms within a small interval in retarded time and compare subtle changes in amplitude. These convergence tests are all done at $r_0 \simeq 12.5M$ using the multiple-mode simulation. In the first plot we fix the number of radial zones at 180 and vary the number of angular zones from 8 to 16 to 32. In the second plot the angular zoning is fixed at 16 and we vary the number of radial zones from 90 to 180 to 290. In going from 90 to 180 radial zones, the wave form changes by at most 10%. In all other cases the maximum relative changes were less than $\sim 5\%$.

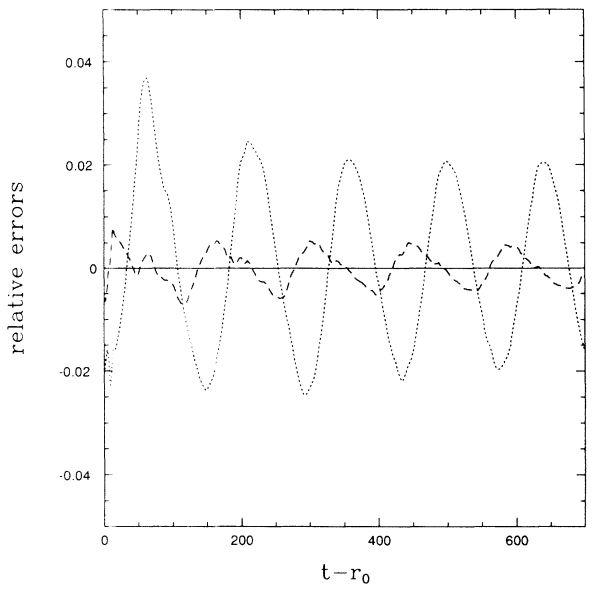

FIG. 5. Relative errors between the wave forms extracted with the template and gauge-invariant methods (dotted) and between those extracted with the Riemann and gauge-invariant methods (dashed). This comparison is made using the multiple-mode run and data from $r_0 \simeq 100M$. The relative errors are plotted as a function of $t-r_0$ (in M).

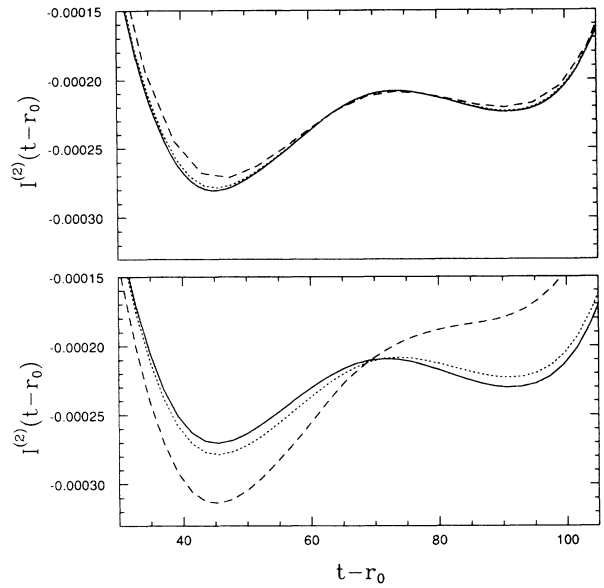

FIG. 6. Convergence of wave forms with increasing grid resolution is shown for a small interval of a multiple-mode wave form. In the upper plot the number of radial zones is fixed at 180 and the number of angular zones is varied from 8 (dashed) to 16 (dotted) to 32 (solid). In the lower plot the number of angular zones is fixed at 16 and the number of radial zones is varied from 90 (dashed) to 180 (dotted) to 290 (solid).

ACKNOWLEDGMENTS

We acknowledge several helpful discussions with K. S. Thorne. This work was supported by the National Center for Supercomputing Applications at the University of Illinois at Urbana-Champaign, and by NSF Grants Nos. PHY 83-08826, AST 85-14911, AST 87-14475, PHY 90-01645, and PHY 90-57865. Calculations were performed at the NSF National Center for Supercomputing Applications. C.R.E. was supported by the Presidential Young Investigator Program.

APPENDIX A: INITIAL VALUES FOR EXTRACTION EQUATIONS

Initial data for numerical simulations on spatial hypersurfaces take the form (γ_{ij},K_{ij}), where γ is the three-metric and K is the extrinsic curvature of the initial time slice. We will show here that it is possible to use these data to determine initial values for the moments appearing in the extraction equations using the gauge-invariant formalism of Sec. II. The procedure is demonstrated for the initial values of the even-parity moments, although it works identically for odd parity.

The gauge-invariant template itself gives us the first necessary initial-value equation:

$$Q_e^{(lm)}(t_0;r_0)=l(l+2)\{I_{lm}^{(l)}(t_0-\epsilon r_0)\}_l \ , \tag{A1}$$

where $Q_e^{(lm)}$ is calculated from the initial three-metric using Eq. (6). Our other starting equation comes from the evolution equation for the three-metric:

$$\partial_t\gamma_{ij}=-2\alpha K_{ij}+D_i\beta_j+D_j\beta_i \ . \tag{A2}$$

Here α is the lapse function ($\alpha\sim 1$ in weak field) and β_i the shift vector. Note that the covariant derivatives D_i in Eq. (A2) are curved-space, spatial covariant derivatives. For this appendix and the rest of this paper, however, our calculations are performed in the weak-field regime where we use flat-space covariant derivatives denoted by ∇_i. Using (A1) and (A2), we obtain

$$\dot{Q}_e^{(lm)}(t_0;r_0)=l(l+2)\{I_{lm}^{(l+1)}\}_l \ , \tag{A3}$$

where $\dot{Q}_e^{(lm)}$ is formed the same way as Eq. (6) except with the first time derivatives of the $A_{\lambda l',lm}$'s. These are defined by

$$\dot{A}_{\lambda l',lm}=\frac{1}{d_{\lambda l',l}}\int d\Omega[-2\alpha K_{ij}(t_0;r_0)+\nabla_i\beta_j(t_0;r_0)+\nabla_j\beta_i(t_0;r_0)](T_{ij}^{\lambda l',lm})^* \ . \tag{A4}$$

To solve for the initial values I and its derivatives, we form l more equations by successively applying I angular-momentum-lowering operators to Eq. (A1). Then we form $l-1$ more equations by applying $l-1$ angular-momentum-lowering operators to Eq. (A3). This gives a total of $2l+1$ equations for I and its first $2l$ time derivatives. We assume that the radiation is either purely incoming or purely outgoing. As an example, for $l=2$ the solution of the five equations yields the initial values for Eqs. (12), (16), and (23):

$$\frac{I^{(2)}(t_0-\epsilon r_0)}{r_0}=-r_0D_2^-Q_e^{(l=2)}+\epsilon r_0^2D_2^-\dot{Q}_e^{(l=2)}+r_0^2D_1^-D_2^-Q_e^{(l=2)} \ , \tag{A5}$$

$$3\frac{I^{(1)}(t_0-\epsilon r_0)}{r_0^2}=r_0\dot{Q}_e^{(l=2)}-2r_0^2D_2^-\dot{Q}_e^{(l=2)}-2\epsilon r_0^2D_1^-D_2^-Q_e^{(l=2)}+3\epsilon r_0D_2^-Q_e^{(l=2)} \ , \tag{A6}$$

and

$$3\frac{I(t_0-\epsilon r_0)}{r_0^3}=Q_e^{(l=2)}-\epsilon r_0\dot{Q}_e^{(l=2)}-2r_0D_2^-Q_e^{(l=2)}+\epsilon r_0^2D_2^-\dot{Q}_e^{(l=2)}+r_0^2D_1^-D_2^-Q_e^{(l=2)} \ . \tag{A7}$$

The angular momentum operators are, of course, purely radial. Therefore, for practical numerical computation of terms such as $D_1^-D_2^-Q_e^{(l=2)}$, the commutation of these operators with the surface integration is exploited.

APPENDIX B: RADIATION EXTRACTION USING THE RIEMANN TENSOR

The Riemann extraction equation [paper I, Eq. (68)] has a drawback from the practical standpoint not discovered until numerical tests were run. The differential operator in the extraction ODE is the second time derivative of the equivalent operator in the other two methods. This unfortunately allowed contamination

of the wave signal by terms constant and linear in time when the ODE was integrated numerically. Here we give an alternative which works much better. Rather than using paper I [Eq. (67b)] directly, we use the trace-free property of the Riemann tensor in a vacuum and obtain

$$\{I^{(2)}(t-r_0)\}_2 = -\tfrac{5}{4}r_0^2\int_0^{\pi/2} d\theta \sin\theta P_2(\cos\theta) R_{trtr} \ . \quad \text{(B1)}$$

It appears that an important criterion for successful matching is that the combination of gravitational field moments be a solution to the radial wave equation. It is possible to find a similar extraction equation for the $l=3$ current moment:

$$\{S^{(4)}(t-r_0)\} = \frac{9r_0}{64}\int_0^{\pi/2} d\theta\, R_{trt\phi} \sin^2\theta(5\cos^2\theta - 1) \ . \quad \text{(B2)}$$

The mass-moment equation (B1) is precisely what one would obtain by considering the real part of the $l=2$ projection of the Weyl tensor component Ψ_2 in the weak field. The odd-parity equation, however, cannot be obtained directly from the imaginary part of the $l=3$ projection of Ψ_2.

For the numerical calculation of the Riemann tensor component, we employ a relation valid in the vacuum, weak-field region (neglecting terms which involve the square of the extrinsic curvature):

$$R_{titj} = {}^3R_{ij} \ , \quad \text{(B3)}$$

where ${}^3R_{ij}$ is the three-dimensional Ricci tensor.

[1] A. M. Abrahams and C. R. Evans, Phys. Rev. D **37**, 318 (1988).
[2] L. Lindblom and S. L. Detweiler, Astrophys. J. Suppl. **53**, 73 (1983).
[3] K. S. Thorne, Rev. Mod. Phys. **52**, 299 (1980).
[4] K. S. Thorne, in *Gravitational Radiation,* edited by N. Dereulle and T. Piran (North-Holland, Amsterdam, 1983).
[5] K. S. Thorne, in *300 Years of Gravitation,* edited by S. W. Hawking and W. Israel (Cambridge University Press, Cambridge, England, 1988).
[6] V. Moncrief, Ann. Phys. (N.Y.) **88**, 323 (1974).
[7] C. W. Misner, K. S. Thorne, and J. A. Wheeler, *Gravitation* (Freeman, San Francisco, 1973).
[8] W. L. Burke, J. Math. Phys. **12**, 401 (1971).
[9] E. N. Glass and L. Lindblom, Astrophys. J. Suppl. **53**, 93 (1983).
[10] C. R. Evans, in *Dynamical Spacetimes and Numerical Relativity,* edited by J. Centrella (Cambridge University Press, Cambridge, England, 1986); Ph.D. thesis, University of Texas at Austin, 1984.
[11] S. L. Detweiler and J. R. Ipser, Astrophys. J. **185**, 685 (1973).
[12] K. S. Thorne, Astrophys. J. **158**, 1 (1969) (see page 7).
[13] B. K. Harrison *et al., Gravitation Theory and Gravitational Collapse* (University of Chicago Press, Chicago, 1965).
[14] See paper I (Ref. 1), Eqs. (55) and (56) and the surrounding discussion.
[15] A. M. Abrahams, in *Frontiers in Numerical Relativity,* edited by C. R. Evans, L. S. Finn, and D. W. Hobill (Cambridge University Press, Cambridge, England, 1989); Ph.D. thesis, University of Illinois at Urbana-Champaign, 1988.